Nano Research Energy

ISSN 2791-0091 (print); 2790-8119 (online)
https://doi.org/10.26599/NRE.2025.9120213

Research Article

A percent-level amide additive for stable aqueous zinc-ion batteries

Liang Huang, Xinxin Cai, Jingchen Tao, Huiquan Zhang, Dongmin Ma, and Weixing Song (✉)

Department of Chemistry, Capital Normal University, Beijing 100048, China

Received: 25 August 2025 / **Revised:** 10 November 2025 / **Accepted:** 23 November 2025 / **Published date:** 4 January 2026

ABSTRACT

The Zn anode/electrolyte interface faces critical challenges, including hydrogen evolution reaction, corrosion, and dendrite growth that degrade battery performance. This study employs 1 mol% N-(2-hydroxyethyl) succinimide (NHS) as a multifunctional electrolyte additive to address these issues. The carbonyl groups (C=O) in NHS can strongly coordinate with Zn atoms and water molecules, selectively adhering to the Zn anode surface to displace H_2O, thereby suppressing parasitic reactions while simultaneously reducing water activity in the electrolyte. The NHS can regulate Zn^{2+} solvation by replacing water molecules in the primary solvation sheath, thereby further facilitating Zn^{2+} desolvation by reducing the number of bound water molecules. Additionally, the NHS on the anode surface enables a homogeneous Zn^{2+} flux, resulting in uniform zinc deposition. As a result, the NHS enables a Zn||Zn symmetric cell to achieve 7,500 h cycling at 1 mA·cm^{-2}, and a Zn||Cu cell to maintain 99.8% Coulombic efficiency over 3200 cycles. The Zn||V_2O_5 full cell retains 82.5% capacity after 7,000 cycles. These findings highlight the proficiency of the NHS in securing Zn anodes for enhanced battery performance.

KEYWORDS

aqueous zinc ion batteries, zinc dendrites, electrolyte additives, solvation sheath

1 Introduction

Aqueous zinc-ion batteries (AZIBs) have gained prominence as a frontrunner for grid-level energy storage solutions, owing to their inherent benefits, such as widespread availability and the impressive theoretical energy capacity of Zn anodes [1–3]. However, Zn anodes face critical challenges, including hydrogen evolution reaction (HER), dendrite growth, and corrosion at the electrolyte interface, which severely compromise cycling stability and lifespan [4–7].

Optimizing the solvation sheath of Zn^{2+} and the anode/electrolyte interface is the key to improved AZIBs performance. The solvent composition dictates zinc ion mobility, conductance, and electrochemical reactivity [8, 9]. Zinc deposition and dissolution benefit from modifying the solvation sheath, boosting stability and reversibility. This minimizes dendrites and improves battery performance [10–12]. The stability of the Zn anode is notably affected by the anode/electrolyte interface [13, 14]. Optimizing this interface can lead to higher Coulombic efficiency and improved cycle life, making it a key factor in the practical application of ZIBs [15–17]. Various techniques have been developed to enhance the robustness of Zn anodes, including surface modifications and structural designs [18–20]. Numerous studies have focused on stabilizing the zinc surface through strategies such as protective coatings (e.g., Sn-Ti_3C_2 [21], SF [22], CuInZIF-8 [23], Sn [24]) and three-dimensional frameworks to control zinc deposition [25–27]. These designs may introduce additional resistance and complexity to the electrode, potentially increasing manufacturing costs [28, 29]. Electrolyte engineering serves as a viable strategy for stabilizing Zn anodes. Conventional additives generally provide limited functionality, primarily acting through either interfacial adsorption on the electrode surface or alteration of Zn^{2+} solvation structures [30, 31]. However, some additives undergo gradual degradation during prolonged cycling due to electrochemical consumption or decomposition, resulting in diminished stabilizing effects over time [32–36].

Herein, we introduce N-(2-hydroxyethyl) succinimide (NHS) as an electrolyte additive to address these challenges. Specifically, the carbonyl groups (C=O) of the NHS not only directly participate in the formation of the Zn^{2+} solvation sheath but also enable the adsorption of NHS molecules onto the anode surface. These two processes are mutually reinforcing, as the regulated solvation structure facilitates more favorable adsorption behavior, while the adsorbed layer, in turn, influences the subsequent desolvation and zinc deposition processes. Thus, the NHS exhibits exceptional molecular stability against electrochemical decomposition while simultaneously delivering triple functionalities: optimizing the electrode/electrolyte interface, restructuring Zn^{2+} solvation sheath, and suppressing the activity of water molecules to stabilize the Zn anode. This study comprehensively demonstrates the efficacy of the NHS as an advanced electrolyte additive for zinc-based batteries. The NHS-

Address correspondence to Weixing Song, songwx@cnu.edu.cn

enabled Zn||Zn symmetric cells achieved enhanced cycling stability (7500 h), while Zn||Cu half-cells maintained an average Coulombic efficiency of 99.8% over 3200 cycles. When integrated with a V_2O_5 cathode, the full cell exhibited outstanding long-term cyclability, retaining 82.5% capacity after 7000 cycles. These results not only elucidate the fundamental mechanisms of NHS in stabilizing Zn anodes but also establish its practical viability for high-performance zinc-ion batteries applications.

2 Experimental

2.1 Materials

$ZnSO_4·7H_2O$ (> 99.0%), vanadium (V) oxide (V_2O_5, >99%), and oxalic acid dihydrate ($C_2H_2O_4$, >99.0%) were purchased from Sigma Aldrich. NHS (97%, N858424) was purchased from Macklin. Zn foil (50 μm, >99.9%), Ti foil (30 μm, >99.9%), and Cu foil were purchased from Tengfeng Metal. Glass fiber separators (Whatman GF/A) and non-woven fabric membranes were purchased from Shenzhen Kejing Star Technology. Deionized water was used to prepare all the aqueous electrolytes. We performed the immersion test under sealed conditions to avoid the influence of air on the results. Our Zn foils are simply polished and cleaned before being placed in an airtight container filled with electrolyte. They are taken out after 10 days and characterized accordingly.

2.2 Fabrication of Zn||Zn symmetric cell

Two 50 μm-thick zinc foils served as the electrodes for a balanced cell configuration. Two different electrolytes (2 M $ZnSO_4$ and 2 M $ZnSO_4$ with NHS), each containing 70 μL, were added to the coin cell, with a piece of glass fiber as the separator.

2.3 Fabrication of Zn-V_2O_5 full cell

In the study, the V_2O_5 was subjected to further thermal processing [37]. A solution of 6 mM V_2O_5 and 30 mM $C_2H_2O_4$ was prepared by dissolving them in 30 mL of deionized water. This mixture was then stirred at a temperature of 70 °C until the water had completely evaporated. The resulting solid material was ground and subjected to calcination at 400 °C for a duration of two hours.

2.4 Characterization

The morphologies of Zn foil anodes were observed by field emission scanning electron microscopy (FESEM, ZEISS Gemini 300), operated at 2 kV and 10 mA. X-ray photoelectron spectroscopy (XPS) measurements were carried out through a Thermo Scientific K-Alpha using monochromatic Al Kα radiation. The crystal structure and material composition information were gathered by X-ray diffraction (XRD, Rigaku, MiniFlex600, Cu Kα), H nuclear magnetic resonance (NMR spectroscopy (Bruker 600 MHz), and Fourier transform infrared spectrometer (Thermo Scientific Nicolet iS20).

2.5 Electrochemical measurements

CR2032 coin cells facilitated aerial assembly of all batteries. Land CT3002A was used to assess the behavior of Zn||Zn symmetric cells and Zn||V_2O_5 full cells behavior. The aqueous electrolyte consisted of 2 M zinc sulfate ($ZnSO_4$), and all electrodes were precision-cut into 12 mm discs. To evaluate Zn anode stability, Zn||Zn symmetric cells were assembled with glass fiber separators. Meanwhile, non-woven fibrous membranes were employed to assess cycling performance under high current density conditions. Coulombic efficiency (CE) measurements along with zinc deposition/stripping profiles were obtained using Zn||Cu half-cell configurations. To characterize the battery capacity and charge/discharge performance, heat-processed V_2O_5 was combined with carbon black and PVDF at a 7:2:1 mass ratio using NMP as a solvent. Subsequently, the slurry was applied uniformly onto the titanium substrate and subjected to drying at 120 °C in a vacuum environment for 12 hours, with a cathode composition of approximately 1.0 mg·cm^{-2} of V_2O_5. Electrochemical impedance spectroscopy (EIS) was conducted with a Corrtest Electrochemical Workstation (Wuhan, China) within the frequency range from 100 kHz to 0.1 Hz. The polarization behavior was analyzed using a standard three-electrode setup, featuring a zinc working electrode, platinum counter electrode, and Ag/AgCl reference electrode. Electrochemical characterization, including Tafel curve measurement and potentiostatic polarization, were conducted on the Corrtest workstation using a three-electrode system at the scan rate of 1 mV·s^{-1} (zinc foil as the working electrode, platinum plate as the counter electrode, and Ag/AgCl as the reference electrode, respectively). CV measurements of Zn||V_2O_5 cells were performed across a 0.2–1.6 V potential window. Real-time observation of zinc deposition morphology in various electrolytes (at 10 mA·cm^{-2} current density) was achieved through *in situ* optical microscopy using a Bresser 52-01005 digital microscope.

2.6 Ionic models and computational methodology

To fine-tune the molecular geometries of NHS solvent molecules, we first performed quantum chemical calculations using Gaussian 16 [38] with the B3LYP/6-311+G(d,p) method. The atomic partial charges for these ions were then determined via the ChelpG scheme, sticking with the same B3LYP functional and 6-311+G(d,p) basis set for consistency. Force field parameters for all ionic and solvent species, formatted according to AMBER conventions, were sourced from established literature [amber-ff] [39]. For water simulations, the SPC/E model saw application. Lorentz-Berthelot rules defined intermolecular cross-interactions.

Two distinct molecular models were developed, with their full specifications outlined in the accompanying table. The atomic-scale simulations were carried out using the GROMACS software suite [40], employing cubic periodic boundary conditions throughout. Atomic trajectories were calculated using the standard Verlet leapfrog integration scheme with a 1.0 femtosecond timestep.

Prior to production runs, each system underwent energy minimization via steepest descent optimization, followed by a gradual cooling protocol from 600 to 300 K over 10 nanoseconds. The systems were then equilibrated under NPT conditions for 20 nanoseconds, with temperature regulated at 300 K by a Nosé-Hoover thermostat (τ = 0.4 ps) and pressure maintained at 1 atmosphere via a Parrinello-Rahman barostat (τ = 0.2 ps). Subsequent 40-nanosecond NVT production runs generated trajectories sampled every 100 femtoseconds for structural and dynamic characterization.

Key solvation configurations were identified through comprehensive atomistic simulations and subsequently used as initial geometries for further DFT computations. These DFT evaluations were executed on the Gaussian 16 platform [gaussian] employing the B3LYP/6-311+G(d) method with Grimme's D3 dispersion correction (gd3bj) to determine binding energies.

Complementary first-principles calculations were conducted using the Vienna *ab initio* Simulation Package (VASP) [vasp] [41],

where electron-ion correlations were simulated using projector-augmented wave (PAW) pseudopotentials [42]. The generalized-gradient approximation (GGA) exchange-correlation functional, specifically the Perdew-Burke-Ernzerhof (PBE) variant, was applied. A plane-wave cutoff energy of 450 eV was enforced, and Γ-centered k-point meshes were utilized for Brillouin zone integration. The exchange-correlation functional included a Gaussian broadening of 0.05 eV, while electronic self-consistency was achieved with a stringent convergence threshold of 1×10^{-5} eV.

The Zn (002) electrode surfaces were modeled with four atomic layers. To mimic the bulk material, the bottom two layers remained fixed during simulations, whereas the top two layers were allowed to relax freely, replicating surface behavior. A 15 Å vacuum layer was incorporated into each system to minimize any unwanted interactions between periodic surfaces.

All configurations underwent full geometric relaxation until reaching equilibrium, with forces converging below 0.01 eV·Å^{-1}. To determine the adsorption energetics, the interactions of both NHS and H_2O molecules with the Zn(002) surface were thoroughly optimized.

3 Results and discussion

To demonstrate the optimal NHS concentration, we prepared electrolytes by adding different concentrations of NHS (0–40 mM) in 2 M $ZnSO_4$. Several batteries using these electrolytes were assembled and tested electrochemically (see Fig. S1 in the Electronic Supplementary Material (ESM)). The Zn||Zn symmetric cells and Zn||Cu half-cells with 20 mM NHS (1 mol%) exhibit the best cycle performance, and this concentration of NHS was selected for further investigation. The protective efficacy of the NHS against corrosion was thoroughly assessed using immersion experiments in $ZnSO_4$ solutions. After 10 days in pure $ZnSO_4$ electrolyte, corrosion emerged substantially on the Zn anode surface. It develops a coarse, ashen texture and uneven, flaky corrosion products (Fig. S2 in the ESM). XRD patterns in Fig. 1(a) reveal the formation of ZnO and by-products $Zn_4SO_4(OH)_6\cdot5H_2O$. These deposits would substantially hinder ion and electron transport across the interface. In striking contrast, zinc samples in NHS-containing electrolyte maintained their metallic luster without detectable corrosion products or ZnO formation, demonstrating effective corrosion inhibition.

Electrochemical measurements further quantified this protective effect. Tafel analysis revealed that the NHS-modified electrolyte reduced the corrosion current density from 7.47 to 6.05 mA·cm^{-2}, while shifting the corrosion potential from −0.973 to −0.961 V (Fig. 1(b)). Taken together, these findings clearly indicate that the NHS provides a two-pronged defense: it prevents

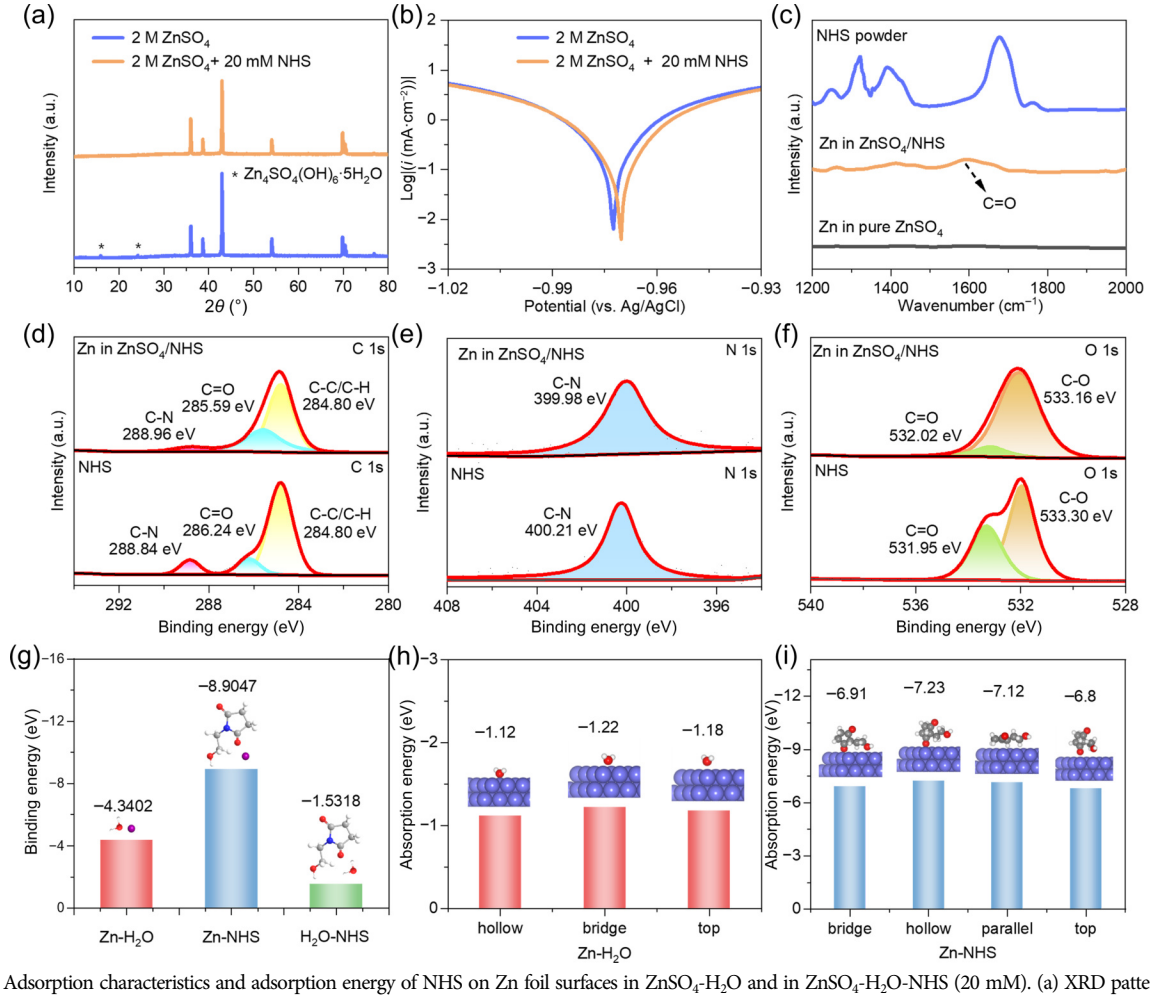

Figure 1 Adsorption characteristics and adsorption energy of NHS on Zn foil surfaces in $ZnSO_4$-H_2O and in $ZnSO_4$-H_2O-NHS (20 mM). (a) XRD patterns of zinc plates following exposure to different electrolytes for 10 days. (b) Polarization curves (collected at 1 mV·s^{-1}) showing the electrochemical behavior of the Zn anode in different electrolyte solutions. (c) FTIR spectra comparing the zinc plate after electrolyte immersion with pure NHS powder. High-resolution XPS spectra of (d) C 1s, (e) N 1s, and (f) O 1s. (g) Calculated binding configurations and energies for Zn-H_2O, Zn-NHS, and H_2O-NHS complexes. DFT-optimized adsorption geometries and corresponding energy profiles for (h) H_2O and (i) NHS molecules on Zn (002) surfaces.

the formation of corrosive byproducts and suppresses electrochemical corrosion at the interface.

The protective mechanism of NHS was investigated through a comprehensive surface analysis of zinc foils immersed in NHS-containing electrolyte. Energy-dispersive X-ray spectroscopy (EDS) confirmed the presence of NHS on the zinc surface through the detection of characteristic C, N, and O elements (Figs. S3 and S4 in the ESM). Fourier transform infrared spectroscopy (FTIR) further demonstrated that the adsorbed NHS retained its molecular structure. The characteristic peaks in the 1200–2000 cm^{-1} range matched those of pristine NHS (Fig. 1(c)). X-ray photoelectron spectroscopy analysis provided additional evidence for NHS adsorption, with distinct C 1s, N 1s, and O 1s signals observed in the high-resolution spectra (Figs. 1(d)–1(f)). These findings collectively demonstrate that the NHS forms a stable protective layer on the zinc surface through molecular adsorption, which is crucial for its corrosion inhibition performance. The observed redshift of the C=O vibrational band in FTIR spectra strongly suggests chemical adsorption of NHS onto the zinc surface, likely through coordination between the carbonyl oxygen and zinc atoms. This chemisorption mechanism was further corroborated by XPS analysis, which revealed significant changes in the electronic environment of NHS functional groups upon surface adsorption. The high-resolution C 1s spectrum showed a notable decrease in C=O peak intensity, accompanied by a substantial chemical shift. This indicates electron density redistribution due to carbonyl-Zn coordination (Fig. 1(d)). Correspondingly, the O 1s spectrum showed a 0.07 eV positive shift in the carbonyl oxygen peak (from 531.95 to 532.02 eV), confirming oxygen's participation in surface bonding (Fig. 1(f)). The N 1s spectrum maintained its characteristic binding energy at 399.98 eV, corresponding to the C–N bond environment (Fig. 1(e)), which served as an internal reference confirming the specificity of the carbonyl-zinc interaction. These spectroscopic findings collectively demonstrate that NHS chemisorbs preferentially through its carbonyl functionality, forming stable coordinate covalent bonds with surface zinc atoms while maintaining the structural integrity of its molecular backbone. The combined FTIR and XPS results provide compelling evidence for this specific adsorption mechanism, which underlies NHS's effectiveness as a corrosion inhibitor [43, 44].

Quantum chemical calculations were carried out to investigate the interaction properties among Zn, H_2O, and NHS molecules. Figure 1(g) presents a comparison of the binding energies for Zn-H_2O, Zn-NHS, and H_2O-NHS. The results reveal that the binding energy of Zn-NHS (−8.9047 eV) is considerably stronger than that of Zn-H_2O (−4.3402 eV). This indicates that Zn has a greater tendency to combine with NHS to form new solvated structures of Zn ions compared to H_2O. Additionally, it is worth mentioning that there is an interaction between H_2O and NHS, as evidenced by their binding energy of −1.53 eV. The interaction between H_2O and NHS occurs via hydrogen bonding between the O–H of H_2O and the C=O of NHS. Additionally, the study examined the adsorption of different solvent molecules on zinc metal surfaces. Figure 1(h) shows that the interaction between Zn and H_2O is relatively weak across various sites, with the most stable bridge structure having an adsorption energy of −1.22 eV. However, the interaction between Zn and NHS is significantly stronger, regardless of whether it's at the top, bridge, hollow, or parallel position on the Zn surface. Notably, the adsorption energy of NHS on Zn at the hollow site reaches up to −7.23 eV, as demonstrated in Fig. 1(i) and Fig. S5 in the ESM.

Understanding the arrangement of solvated ions is crucial to grasping their electrochemical behavior, which is precisely why we investigated the impact of the NHS on such configurations. In a solvation shell, the polar carbonyl group in NHS can disrupt the Zn^{2+} hydration shell by competing with and replacing the water molecules currently attached. To verify this hypothesis, we conducted nuclear magnetic resonance (NMR) and FTIR analyses. In the NMR result, the ^1H peak of pure H_2O in DMSO-d_6 initially appeared at 3.33 ppm (Fig. S6 in the ESM). Upon adding $ZnSO_4$, the peak significantly shifts to a higher position at 3.70 ppm (Fig. 2(a)), indicating a tight coordination of water molecules with Zn^{2+}, which decreases the free water and diminishes proton shielding. The carbonyl oxygen of NHS is expected to coordinate with Zn^{2+} and solvated water to regulate its solvation sheath. Moreover, the NHS can reduce the number of active water molecules by forming hydrogen bonds with free H_2O, weakening the proton shielding effect and inducing larger chemical shifts compared to pure H_2O. When the NHS is introduced into the $ZnSO_4$ electrolyte (5–40 mM), the peak gradually shifts from 3.70 ppm to 3.66 ppm, suggesting an increase in electron density on hydrogen. This shift could arise from either the NHS entering the Zn^{2+} solvation sheath, which interacts with and releases the solvated water, or interactions between free H_2O molecules and NHS. To distinguish between these possibilities, we examined the H_2O-NHS interaction in the absence of $ZnSO_4$ [45]. Opposite to the trend observed in the $ZnSO_4$ system, the ^1H peak shifts from 3.605 ppm to a lower position of 3.633 ppm following the concentration change in NHS (5–40 mM) (Fig. 2(b)). This reflects the reduction in electron density of the H atoms, which can be attributed to the increasing content of NHS molecules, thereby enhancing both the intermolecular interactions between water molecules and between water molecules and NHS molecules. These contrary findings in two solution systems rule out free NHS-H_2O interactions as the cause of the initial peak blueshift from 3.33 to 3.7 ppm and the subsequent redshift to 3.66 ppm, implying that NHS releases the solvated water, thus regulating the Zn^{2+} solvation sheath.

FTIR spectroscopy provided additional evidence. The coordination of the NHS with Zn ions and free water molecules not only regulates the Zn^{2+} solvation structure but also influences the SO_4^{2-}. In a pure $ZnSO_4$ aqueous solution, the SO_4^{2-} exhibits a vibrational stretching peak at 1077 cm^{-1}. Upon adding NHS (2 M $ZnSO_4$ + 40 mM NHS), this peak blueshifts to 1096 cm^{-1} (Fig. 2(c)), indicating the coordinated NHS molecules with a large steric hindrance might squeeze the solvated SO_4^{2-}, thus reducing the constraint on SO_4^{2-} [46].

Single NHS anion inclusion within the solvation sheath, displacing a water molecule, notably reduced the electrostatic potential (Figs. 2(d) and 2(e)). This reduction suggests weaker repulsive forces between solvated structures and a diminished positive charge, facilitating faster Zn^{2+} diffusion. Additionally, the strong binding energy between NHS and Zn^{2+} makes the desolvation of hydrated Zn^{2+} in the new bilayer more favorable than in pure $ZnSO_4$ electrolyte, promoting faster interfacial Zn^{2+} transfer. Electrostatic potential (ESP) mapping further supports this mechanism: NHS exhibits a higher local electronegativity (−3.41 eV) compared to H_2O (−2.21 eV) (Fig. 2(f)), which explains its preferential coordination with Zn^{2+}. Although the NHS concentration is much lower than Zn^{2+}, meaning many ions remain fully hydrated, $[Zn(H_2O)_6]^{2+}$ migrating toward the anode can still reorganize. Upon approaching the interface, it may transform into a new coordination structure involving the NHS and fewer water molecules.

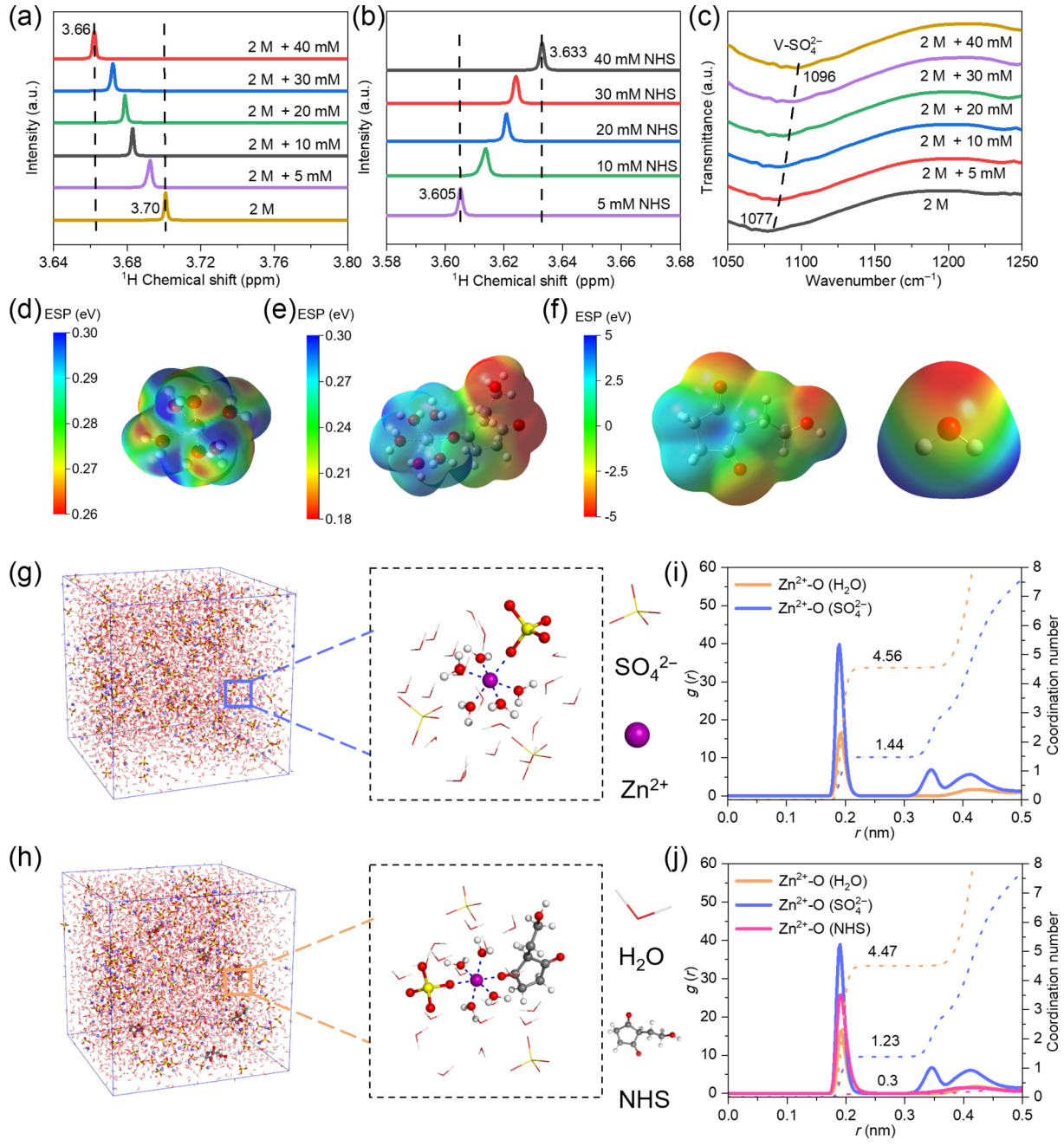

Figure 2 Regulation of the solvation sheath of Zn^{2+} by the addition of NHS. (a) ^{1}H NMR spectra of 2 M $ZnSO_4$ electrolytes with different contents of NHS. (b) ^{1}H NMR spectra of NHS-H_2O with different contents of NHS in H_2O. (c) FTIR spectra of 2 M $ZnSO_4$ electrolytes with different contents of NHS. Electrostatic potential mapping of (d) the original Zn^{2+}-6H_2O solvation structure and (e) Zn^{2+}-5H_2O-NHS. (f) Electrostatic potential mapping of NHS and H_2O. Molecular dynamics simulations provide three-dimensional visualizations of: (g) $ZnSO_4$-H_2O, and (h) $ZnSO_4$-H_2O-NHS, alongside close-up views of Zn^{2+} solvation structures (NHS concentration: 20 mM). The simulated radial distribution functions and Zn^{2+}-O coordination numbers are plotted for: (i) in $ZnSO_4$-H_2O, and (j) in $ZnSO_4$-H_2O-NHS.

MD simulations were used to compare Zn^{2+} solvation evolution in pure $ZnSO_4$ and NHS-containing electrolytes. Considering the optimal cyclic performance of batteries with various NHS contents, the electrolyte with 20 mM NHS was conducted to build the MD simulation model. In pure $ZnSO_4$ (Fig. 2(g)), Zn^{2+} coordinates with five H_2O molecules and one SO_4^{2-}, forming $[Zn(H_2O)_5(SO_4)]$. In contrast, the NHS-containing system (Fig. 2(h)) shows NHS displacing one H_2O molecule in the solvation shell due to its greater steric hindrance. Radial distribution functions (RDFs) and coordination number analysis corroborate this finding. The RDF for pure $ZnSO_4$ (Fig. 2(i)) displays a sharp Zn–O(H_2O) peak at 1.92 Å, with an average hydration number of 4.56, consistent with the $[Zn(H_2O)_5(SO_4)]$ structure. In the NHS-modified electrolyte, an additional Zn–O (NHS) peak appears at a similar position (Fig. 2(j)), confirming NHS incorporation into the Zn^{2+} solvation shell. Quantitatively, the average Zn–O (H_2O) coordination number decreases from 4.56 to 4.47, while Zn–O (NHS) coordination increases to 0.3. Moreover, the decrease in the average Zn–O (SO_4^{2-}) coordination number also indicates the easier SO_4^{2-} desolvation from the Zn^{2+} solvation sheath. This is consistent with the previous discussion in Fig. 2(c) that the coordinated NHS molecules with a large steric hindrance might release the solvated SO_4^{2-}. Thus, the dominant solvated structure shifts to $[Zn(H_2O)_4(NHS)(SO_4)]$, demonstrating

NHS's ability to regulate ligand water numbers and reshape the Zn^{2+} solvation environment.

Additionally, although the Zn^{2+} coordination number shows that the NHS only weakly participates in the construction of the Zn^{2+} solvation structure, these subtle changes accumulate to facilitate the desolvation of Zn^{2+} and easier Zn deposition, further expanding the cyclic performance of the Zn anode in the NHS-containing electrolyte.

NHS plays a dual role in zinc-ion batteries by modifying both the solvated structure and the electrolyte/electrode interface. To elucidate its binding affinity to the Zn surface, we analyzed molecular orbital energy levels. The lowest unoccupied molecular orbital (LUMO) of NHS (−0.064 eV) lies below that of H_2O (0.016 eV) (Fig. 3(a)), indicating that the NHS can accept electrons and prefer to coordinate with Zn atoms. Furthermore, the Zn-$5H_2O$-NHS complex exhibits a higher highest occupied molecular orbital (HOMO) energy (−0.4529 eV) compared to Zn-$6H_2O$ (−0.6576 eV) (Fig. S7 in the ESM), suggesting that adsorbed Zn-$5H_2O$-NHS more readily donates electrons upon interaction with the Zn foil.

Charge density distribution analysis reveals significant electron transfer at the Zn/NHS (H_2O) interface. In the Zn(002)-H_2O model, minimal electron sharing is observed (Fig. 3(b)), whereas the Zn (002)-NHS configuration shows strong electron cloud overlap between Zn and the carbonyl oxygen (O) of NHS (Fig. 3(c)). This enhanced electron density around the C=O group aligns with prior XPS results, proving that adsorption is driven primarily by chemical interactions between Zn and the NHS carbonyl group [47]. Consistent with these findings, contact angle measurements demonstrate improved wettability of the NHS-containing electrolyte on Zn foil (Fig. 3(d)), reflecting stronger interfacial adsorption.

To probe the zinc deposition mechanism, we evaluated nucleation overpotentials using CV tests. The NHS-modified electrolyte exhibits a lower nucleation overpotential (Fig. 3(e) and Fig. S8 in the ESM), indicating a reduced energy barrier for Zn nucleation. Chronoamperometry (CA) tests at −150 mV further elucidate the deposition dynamics. With pure $ZnSO_4$, the current density keeps climbing after 100 seconds (as shown in Fig. 3(f)), indicating that Zn^{2+} spread out in two dimensions across the electrode surface for quite a while. This sideways movement encourages Zn^{2+} to accumulate on small bumps, and that eventually triggers dendrite growth (see Fig. S9 in the ESM).

In comparison, the electrolyte with NHS shows a stable current density for 50 seconds, followed by a slow increase. This suggests the three-dimensional diffusion on the Zn anode. We propose that NHS adsorbs preferentially at initial zinc nucleation sites. This restricts Zn^{2+} surface diffusion and suppresses two-dimensional

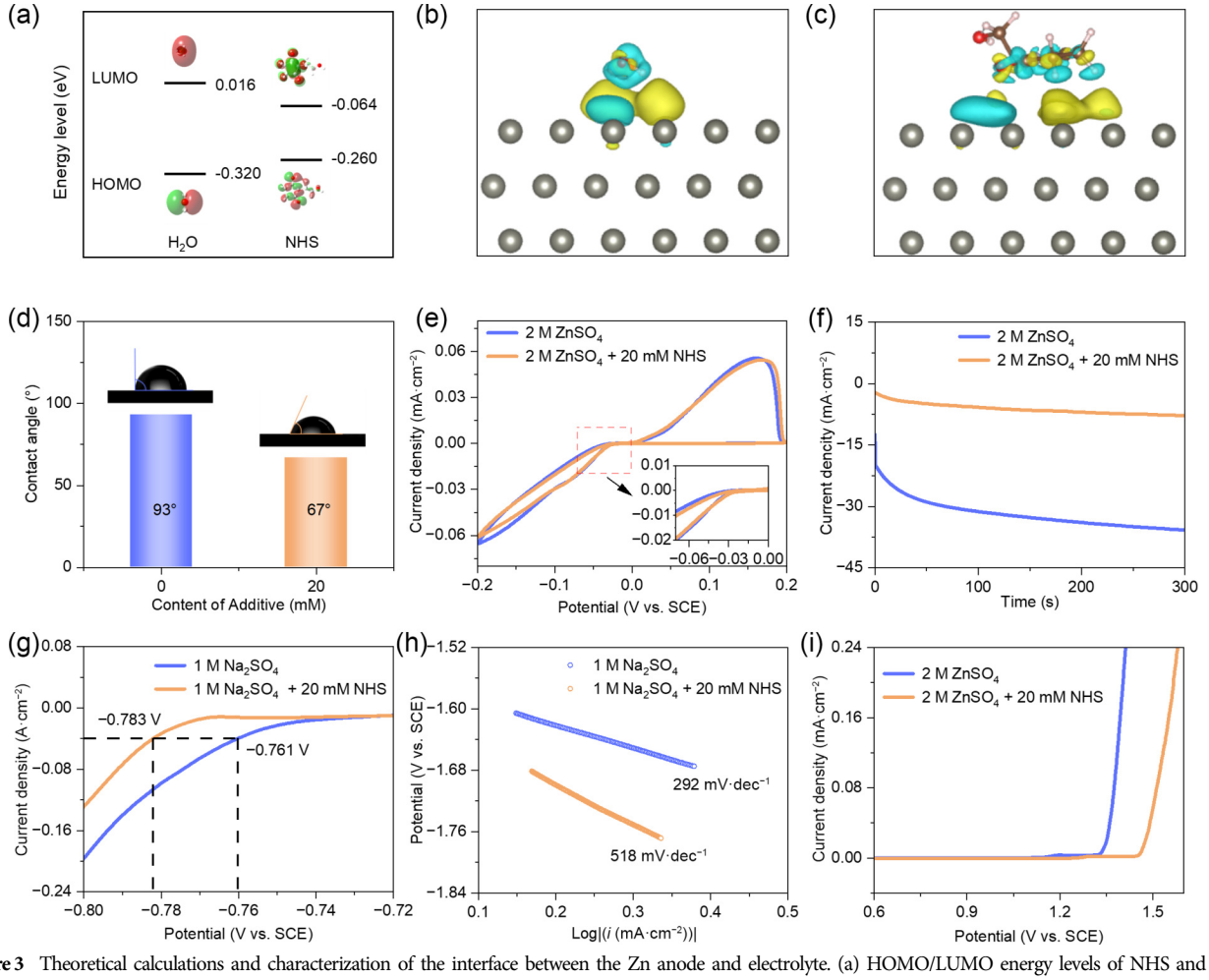

Figure 3 Theoretical calculations and characterization of the interface between the Zn anode and electrolyte. (a) HOMO/LUMO energy levels of NHS and H_2O molecules. (b) and (c) Spatial distributions of charge density difference between Zn and H_2O or NHS (Clusters of yellow and cyan represent heightened and diminished electron density, respectively). (d) Contact angles of $ZnSO_4$-H_2O and $ZnSO_4$-H_2O-NHS on Zn foil surface. (e) CV curves of Zn||Cu half-cells at a scan rate of 1 mV·s^{-1}. (f) Chronoamperograms of $ZnSO_4$-H_2O and $ZnSO_4$-H_2O-NHS at −150 mV overpotential. (g) LSV curves with three-electrode configuration in $ZnSO_4$-H_2O and in $ZnSO_4$-H_2O-NHS. (h) Related Tafel plots. (i) OER potentials used Zn||Cu cells at a 1 mV·s^{-1} scan rate.

spreading. As a result, Zn^{2+} is reduced *in situ*, resulting in smooth and uniform deposition without obvious dendrite formation. This behavior is attributed to the preferential adsorption of NHS molecules on the Zn anode, which reduces water-induced side reactions and promotes a homogeneous distribution of Zn^{2+}. Moreover, the reduced desolvation barrier of the NHS-regulated solvation structure lowers the nucleation overpotential, thereby promoting uniform nucleation and suppressing the rampant dendritic growth observed in the additive-free electrolyte.

Electrochemical studies using linear scanning voltammetry on Zn||Cu cells unveiled distinct behaviors across various electrolytes (Fig. 3(g)). Specifically, the presence of NHS in the electrolyte yielded a reduced hydrogen evolution reaction (HER) onset potential of −0.783 V vs. SCE at a current density of 1 $mA·cm^{-2}$, as opposed to the pure Na_2SO_4 electrolyte, which registered −0.761 V vs. SCE at the same current density. This discrepancy highlights the effectiveness of the NHS in reducing water consumption. This HER inhibition was further analyzed by Tafel curves (Fig. 3(h)), where the NHS-modified electrolyte shows a significantly higher Tafel slope (518 $mV·dec^{-1}$) than the pure Na_2SO_4 system (292 $mV·dec^{-1}$), indicating slower HER kinetics. Furthermore, as the NHS concentration grew in the $ZnSO_4$-based electrolytes, we observed a corresponding rise in the oxygen evolution potential, as illustrated in Fig. 3(i) and Fig. S10 in the ESM within the supplementary materials. This rise widened the electrochemical stability window. The combo of repressed hydrogen evolution and boosted oxygen evolution potential made a big difference, enhancing the system's overall electrochemical stability considerably.

Microscopic analysis of Zn anode surfaces via scanning electron microscopy (SEM) was conducted at 1 $mA·cm^{-2}$ across cycling intervals to clarify zinc plating behavior. Striking differences were observed between the two electrolyte systems [48]. In the $ZnSO_4$ electrolyte, the anode surface develops progressively rougher morphology with cycling. After 10 cycles, randomly oriented flake-like deposits of varying sizes emerge (Fig. 4(a) and Fig. S11 in the ESM). This inhomogeneous growth intensifies after 200 cycles, resulting in a highly porous and disordered structure. Cross-sectional analysis revealed excessive Zn accumulation exceeding 30 μm in thickness (Fig. 4(e)), indicative of uncontrolled deposition. Conversely, the NHS-modified electrolyte promotes uniform Zn plating. As shown in Fig. 4(b), the anode surface maintained a compact and smooth morphology throughout cycling from the initial 10 to 200 cycles. The deposited Zn layer exhibited exceptional homogeneity with a well-controlled thickness of approximately 9 μm (Fig. 4(f)). This dense packing was further confirmed in side-view observations after 50 cycles at higher current density (5 $mA·cm^{-2}$ and Fig. S12 in the ESM).

The real-time optical microscopy observations provided further insight into the zinc deposition behavior (Fig. S13 in the ESM). In the baseline $ZnSO_4$ electrolyte, non-uniform nucleation became evident during electroplating, with subsequent growth exhibiting clear dendritic characteristics (Fig. 4(c)). This pattern aligns with the well-documented "tip effect", where Zn^{2+} preferentially deposits on existing protrusions, leading to accelerated growth at these sites. In striking contrast, the NHS-modified electrolyte produced fundamentally different deposition behavior. The zinc foil maintained exceptional morphological homogeneity throughout the plating process, demonstrating both improved nucleation uniformity and long-term stability (Fig. 4(d)). These observations provide direct visual evidence that NHS additives effectively regulate initial nucleation while completely suppressing dendritic growth mechanisms. The contrast between the two systems underscores the dual functionality of the NHS in modifying nucleation processes and preventing dendrite formation. This transformative effect on deposition morphology offers compelling evidence for the role of the NHS in enabling stable zinc electrodeposition, addressing one of the key challenges in zinc-based battery systems. The improved deposition behavior can be attributed to the ability of the NHS to homogenize the electric field distribution and regulate ion flux at the electrode-electrolyte interface.

The combined experimental and theoretical evidence reveals a comprehensive mechanism of NHS action in zinc deposition systems. In the conventional $ZnSO_4$ electrolyte, the predominant $[Zn(H_2O)_5SO_4]$ solvation structure introduces numerous activated water molecules to the electrode interface. These water molecules actively compete with Zn^{2+} for electrons, triggering undesirable side reactions that compromise deposition quality (Fig. 4(g)). The introduction of the NHS fundamentally alters this dynamic by modifying the solvation structure. NHS replaces one water molecule in the coordination sphere (Fig. 4(h)), thereby reducing the availability of reactive water molecules at the interface. This structural modification simultaneously achieves two critical effects: suppression of parasitic side reactions and promotion of uniform zinc deposition.

Electrochemical performance evaluation across different electrolyte concentrations proves these mechanistic insights. Zn||Zn symmetric cells employing the optimized 20 mM NHS-containing electrolyte demonstrate superior reversibility, achieving a 250-hour cycle life with stable 145 mV voltage hysteresis at 10 $mA·cm^{-2}$ (Fig. S14 in the ESM). Past this ideal point, greater polarization emerges, attributed to higher charge transfer resistance, notably in Zn||Cu half-cells. While the baseline $ZnSO_4$ electrolyte suffers from rapid capacity fade and fluctuating Coulombic efficiency (CE) within 400 cycles at 5 $mA·cm^{-2}$, the NHS-modified system maintains improved stability for over 3200 cycles with a consistent 99.4% Coulombic efficiency (Figs. S15 and S16 in the ESM). This improvement directly correlates with the NHS's ability to prevent dendritic short-circuiting while ensuring highly reversible zinc plating/stripping. The comprehensive dataset consistently points to 20 mM NHS as the optimal concentration, balancing solvation structure modification with minimal polarization effects. This concentration was therefore selected for all subsequent investigations in this study.

In order to investigate the effect of different NHS concentrations on electrolyte properties and zinc deposition/stripping behavior, electrochemical impedance tests were carried out on symmetric cells with varying NHS concentrations before and after cycling. Analysis of the Nyquist plots reveals a progressive enlargement of semicircle diameters with increasing NHS concentration compared to the pure $ZnSO_4$ electrolyte (Fig. S17 in the ESM). Significantly, the absence of additional semicircles in the high-frequency region after cycling confirms that no secondary interfacial layer formed on the zinc electrode surface. Long-term galvanostatic cycling tests were conducted on Zn||Zn symmetric cells at a current density of 1 $mA·cm^{-2}$ with an areal capacity of 1 $mAh·cm^{-2}$. As shown in Fig. 5(a), the cell employing pure $ZnSO_4$ electrolyte exhibited an abrupt and irreversible voltage drop after 1200 hours of operation. The occurrence can be attributed to zinc dendrites piercing the separator, causing internal shorts. Notably, the $ZnSO_4$ electrolyte with the NHS additive exhibited remarkably improved cycling performance, running continuously for more than 7500 hours

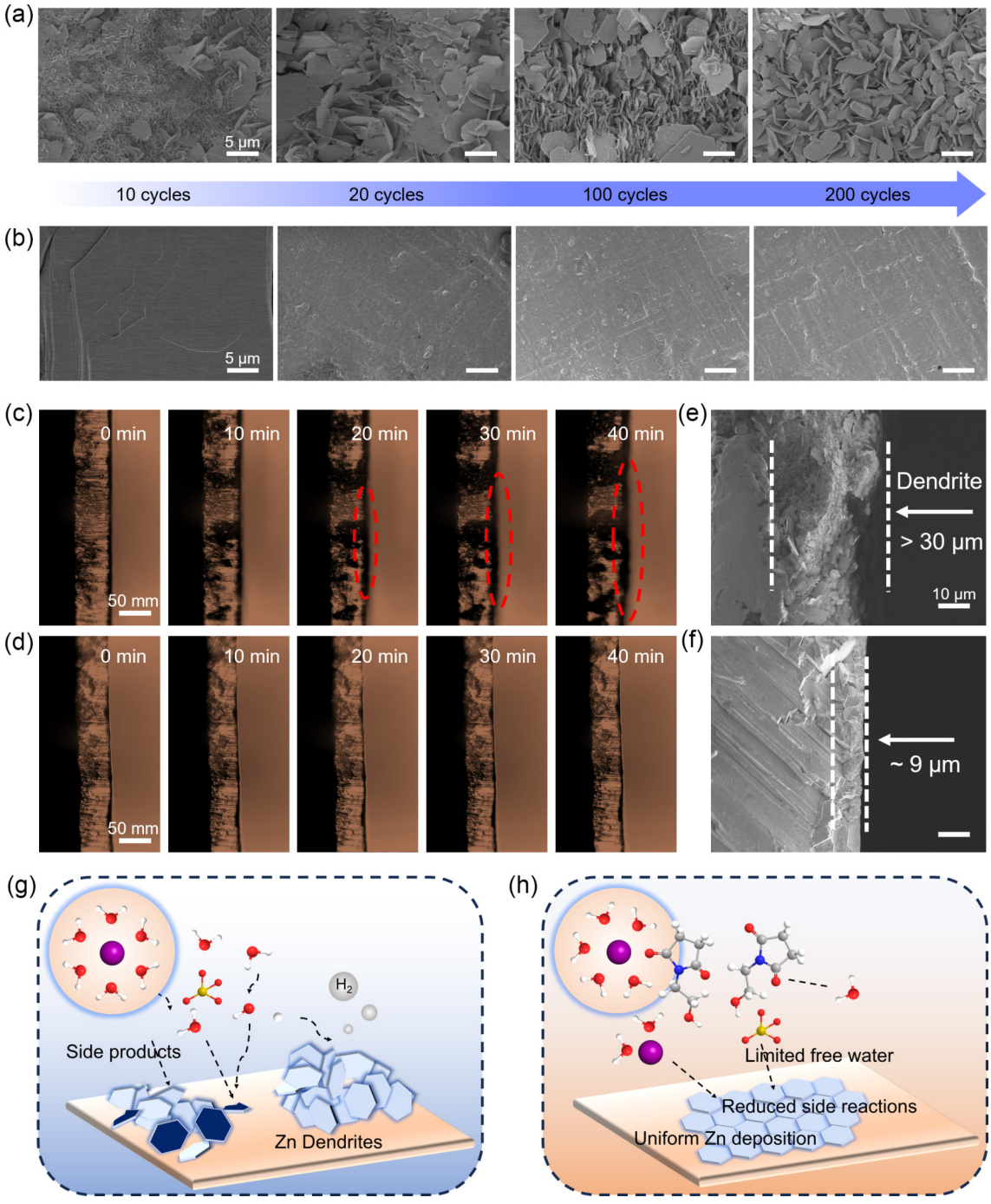

Figure 4 Comparison of characterization of Zn plating/stripping behaviors upon cycles. SEM images of the deposition morphology of Zn anodes: (a) in $ZnSO_4$-H_2O and (b) in $ZnSO_4$-H_2O-NHS (20 mM) after 10, 20, 100, and 200 cycles at 1 mA·cm^{-2} for 1 mAh·cm^{-2}. *In situ* optical microscopic images of the Zn deposition morphology on the surface (c) in $ZnSO_4$-H_2O and (d) in $ZnSO_4$-H_2O-NHS 10 mA·cm^{-2}. Cross-sectional SEM images of Zn anodes (e) in $ZnSO_4$-H_2O and (f) in $ZnSO_4$-H_2O-NHS in symmetric cells after 200 cycles at 1 mA·cm^{-2} for 1 mAh·cm^{-2}. (g, h) Schematic illustration of the underlying mechanism of enhanced electrochemical performance by NHS.

without failure. What's more, the voltage hysteresis in the NHS-treated system progressively decreased before leveling off at just 51 mV, a clear indication of enhanced stability. The evaluation of Zn||Zn symmetric cells' shelving and recovery functions, using alternating cycling and rest cycles, was performed to assess their stability (Fig. 5(b)). The cell with NHS-modified $ZnSO_4$ electrolyte demonstrated exceptional cycling stability over 4300 h, maintaining a low average overpotential of 55 mV. Alternatively, the $ZnSO_4$ electrolyte cell demonstrated considerable voltage variations and experienced a short circuit prematurely, within just 500 hours. These results confirm that the NHS additive significantly stabilizes the Zn electrode, enabling prolonged cycling. SEM analysis also indicated sustained uniform Zn deposition/stripping within NHS-containing cells during extended cycling at 5 mA·cm^{-2} and 2.5 mAh·cm^{-2} (Figs. S18 and S19 in the ESM). The failure of the symmetric cell after 7500 hours may be attributed to the localized growth of dendrites (Fig. S20 in the ESM). Additionally, rate capability tests (0.5–10 mA·cm^{-2}) demonstrated that cells with 20 mM NHS exhibited superior and more stable performance compared to the additive-free

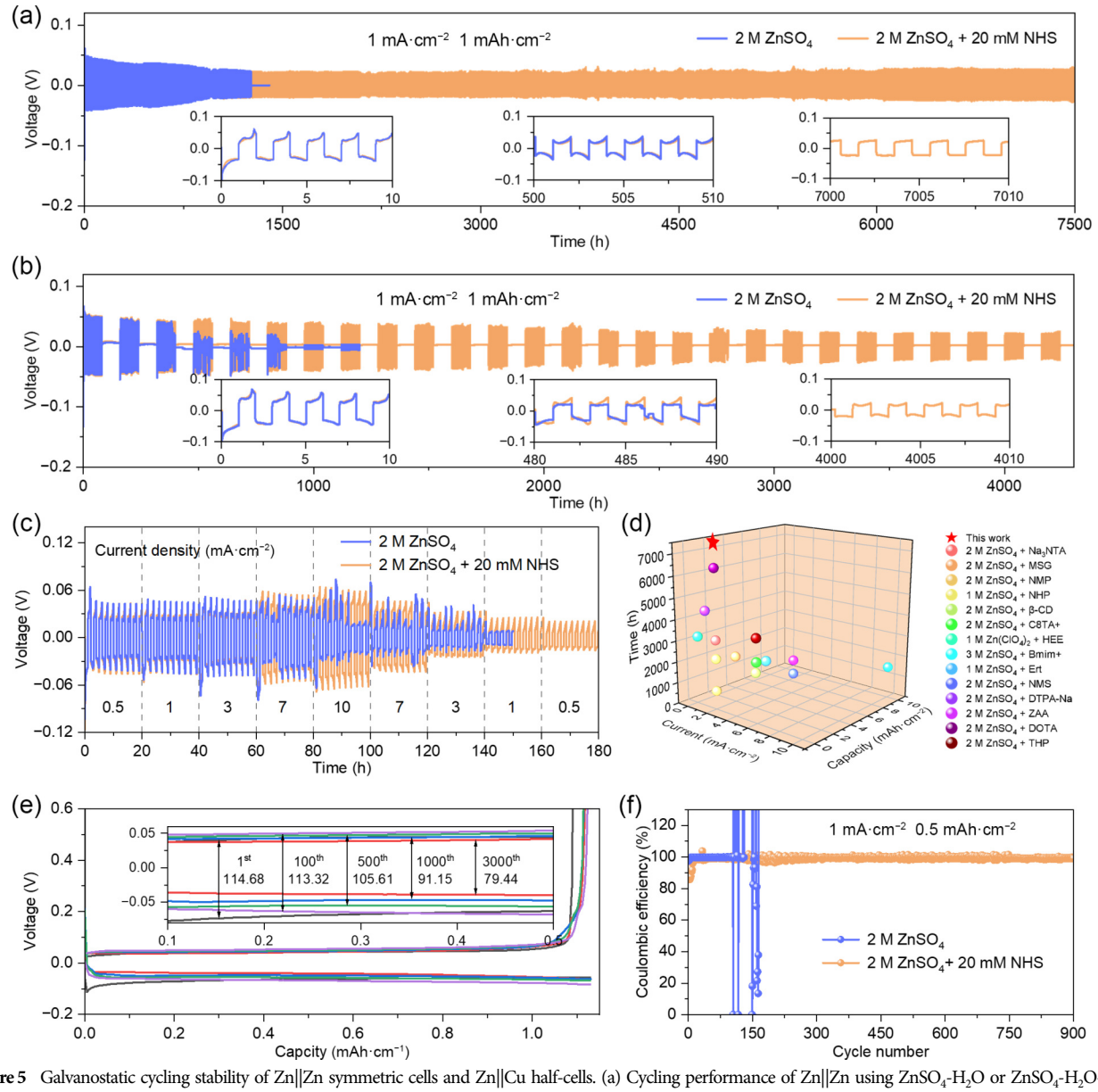

Figure 5 Galvanostatic cycling stability of Zn||Zn symmetric cells and Zn||Cu half-cells. (a) Cycling performance of Zn||Zn using $ZnSO_4$-H_2O or $ZnSO_4$-H_2O-NHS (20 mM) as the electrolyte at 1 mA·cm^{-2} for 1 mAh·cm^{-2}. (b) Dynamic measurement of Zn||Zn symmetric cell with a combination of Zn stripping/plating cycling (80 h) and resting (80 h) at 1 mA·cm^{-2} for 1 mAh·cm^{-2}. (c) Zn||Zn cell rate capability at different current densities. (d) Cumulative capacity comparison of Zn||Zn cells with varied electrolyte additives. (e) Voltage-capacity diagrams of Zn||Cu half-cells in $ZnSO_4$-H_2O-NHS at various cycles. The insert shows the amplification at different cycles between 0.1 and 0.5 mAh. (f) Cycling performance of Zn||Cu using $ZnSO_4$-H_2O or $ZnSO_4$-H_2O-NHS as the electrolyte at 1 mA·cm^{-2} for 1 mAh·cm^{-2}.

electrolyte (Fig. 5(c)). This enhanced rate tolerance further underscores the effectiveness of the NHS in suppressing Zn dendrite growth and sustaining long-term anode stability. When benchmarked against recently reported electrolyte additives, NHS stands out for its good electrochemical stability (Fig. 5(d) and Table S1 in the ESM) and remarkable efficiency at a low concentration, demonstrating enhanced performance compared to additives that typically require higher concentrations to achieve similar effects. These findings highlight the critical role of the NHS in mitigating Zn dendrite formation and improving the cycling durability of Zn-based batteries.

The voltage profiles of the Zn||Cu half-cell demonstrate improved cycling stability (Fig. 5(e)), with the plating/stripping voltage gap gradually decreasing over time, indicating enhanced reaction reversibility. Notably, the potential gap remains nearly constant during the initial 100 cycles, likely due to an inhomogeneous electric field caused by the inherent electrode surface roughness, which leads to incomplete reactions and a smaller initial polarization. When operated at 1.0 mA·cm^{-2} with 0.5 mAh·cm^{-2}, the zinc-copper cell using basic $ZnSO_4$ electrolyte shows erratic charge efficiency and breaks down within a mere 100 charge-discharge cycles. The root cause lies in the unchecked formation of zinc dendrites, which ultimately leads to cell failure. In contrast, the cell with 20 mM NHS-modified $ZnSO_4$ electrolyte displays significantly improved reversibility, sustaining an average Coulombic efficiency of 99.8% over 900 cycles (Fig. 5(f)).

The impact of NHS inclusion on Zn||V_2O_5 cell electrochemistry was assessed to determine the viability of using NHS in real-world applications by contrasting cell performance in $ZnSO_4$ solutions, with and without NHS. (Fig. S21 in the ESM). At a high current density of 10 A·g^{-1}, the cell with pure $ZnSO_4$ electrolyte suffered rapid capacity degradation, declining from 210.3 to 135.7 mAh·g^{-1} after 1600 cycles (64.5% retention). On the flip side, the electrolyte

with NHS really gave the cycling stability a shot in the arm. After a whopping 7000 cycles, it was still kicking with 82.5% of its original capacity (dropping from 195.6 to 161.4 mAh·g^{-1}), all while keeping a stellar Coulombic efficiency of 99.5% (Fig. 6(a)). Similar improvements were observed at 5 A·g^{-1}, where the NHS-modified cell delivered a stable capacity of 194.4 mAh·g^{-1} after 3000 cycles, far outperforming the additive-free system (Fig. S22 in the ESM). Further tests at 1 A·g^{-1} (Fig. 6(b) and Fig. S23 in the ESM) confirmed that the addition of 20 mM NHS substantially improved capacity retention, with cells retaining 95% of their initial capacity after 300 cycles in 2 M $ZnSO_4$ electrolyte. Additionally, the NHS-modified cells exhibited superior rate capability (Fig. 6(c)), demonstrating excellent capacity recovery when cycled at varying current densities (0.1 → 5 → 0.1 A·g^{-1}). The average specific capacities at 0.1, 0.2, 0.5, 1, and 5 A g^{-1} were 330.7, 285.7, 258.1, 240.5, and 199.8 mAh·g^{-1}, respectively (Fig. S24 in the ESM). In comparison, cells with pure $ZnSO_4$ suffered rapid capacity decay, particularly at elevated current densities, highlighting the important role of NHS in stabilizing Zn deposition and improving reaction kinetics CV analysis further confirmed the enhanced reversibility of the NHS-modified system (Fig. 6(d)). The 5th cycle CV curves exhibited two well-defined redox couples, corresponding to the V^{3+}/V^{4+} and V^{4+}/V^{5+} transitions during charge/discharge. Notably, the cell with the NHS additive

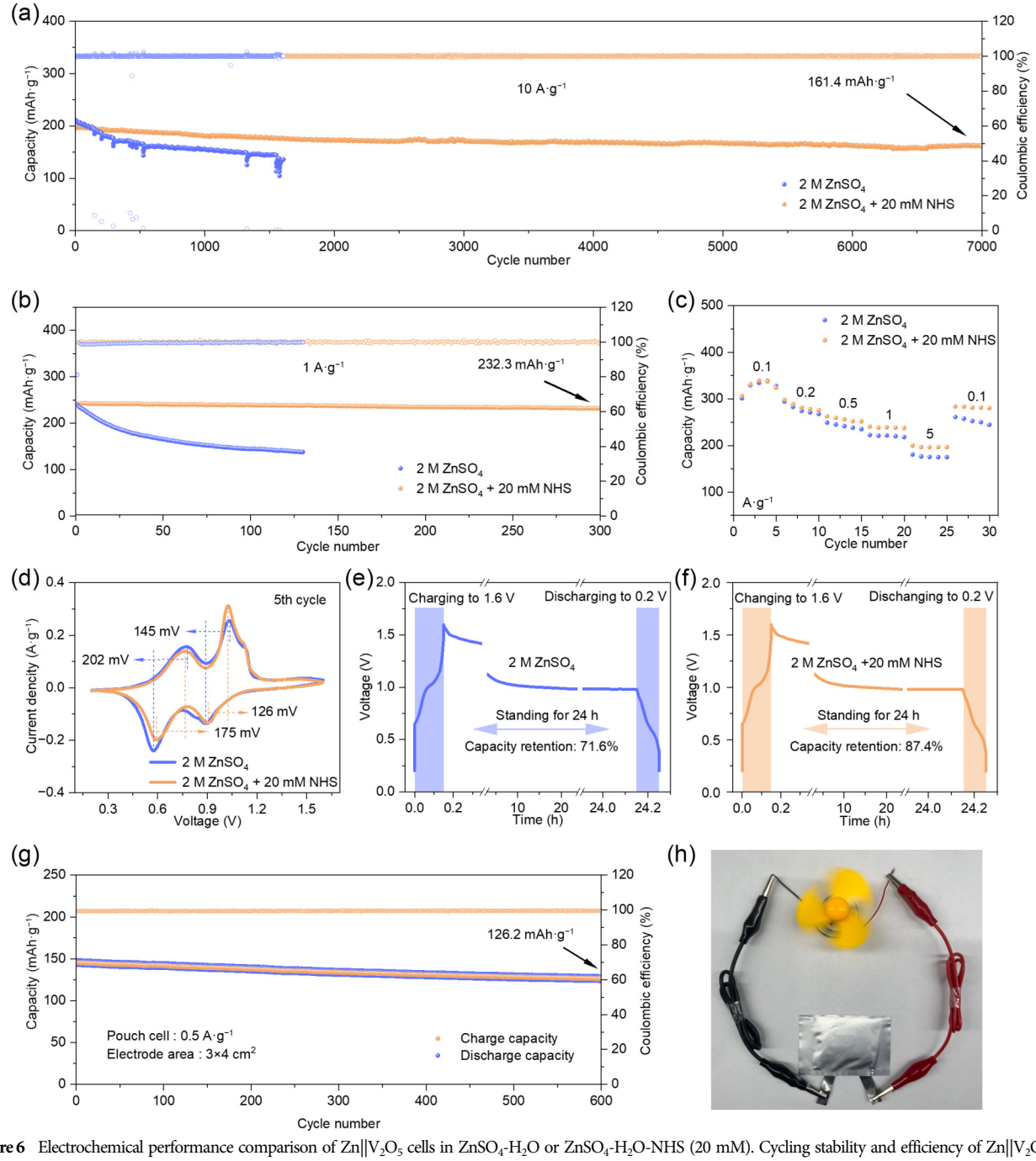

Figure 6 Electrochemical performance comparison of Zn||V_2O_5 cells in $ZnSO_4$-H_2O or $ZnSO_4$-H_2O-NHS (20 mM). Cycling stability and efficiency of Zn||V_2O_5 full cell at (a) 10 A·g^{-1} and (b) at 1 A·g^{-1}. (c) Rate performance of Zn||V_2O_5 full cell in $ZnSO_4$-H_2O or $ZnSO_4$-H_2O-NHS. (d) Voltammetry tracings obtained at a scanning velocity of 0.1 mV·s^{-1}. Galvanostatic cycling of Zn||V_2O_5 cells using (e) $ZnSO_4$-H_2O or (f) $ZnSO_4$-H_2O-NHS (1 A·g^{-1}, charged to 1.6 V, and discharged to 0.2 V after standing for 24 h). (g) Cycling stability and efficiency of Zn||V_2O_5 pouch cell at 0.5 A·g^{-1} in $ZnSO_4$-H_2O·NHS. (h) Optical image of a powered fan turning by a Zn||V_2O_5 pouch cell.

displayed significantly reduced electrode polarization compared to the pure $ZnSO_4$ system, corroborating its improved reaction kinetics and cycling stability. Incorporating the NHS into the $ZnSO_4$ electrolyte significantly suppresses the self-discharge activity in Zn||V_2O_5 cells. After 24 hours of open-circuit rest, the NHS-modified cell retains 87.4% of its initial capacity, significantly exceeding the 71.6% retention of the pure $ZnSO_4$ system (Figs. 6(e) and 6(f)). This improvement stems from the protective adsorption of NHS molecules on the Zn anode surface, which suppresses parasitic reactions, including hydrogen evolution and corrosion. NHS preferentially adsorbs at nucleation sites over H_2O molecules, thereby inhibiting water decomposition and associated side reactions.

Flexible pouch cells fabricated with NHS-modified electrolyte demonstrate stable cycling over 300 cycles at 0.5 $A{\cdot}g^{-1}$, maintaining a specific capacity of 126.2 $mAh{\cdot}g^{-1}$ (Fig. 6(g)). The voltage of the pouch battery was measured to be 1.101 V with a voltmeter (Fig. S25 in the ESM). Visual inspection reveals striking differences between cells with and without NHS additives: control cells exhibit noticeable swelling after cycling. In contrast, NHS pouch cells maintain structural integrity, directly evidencing suppressed gas-evolving side reactions (Fig. S26 in the ESM). The redesigned NHS pouch cell demonstrates real-world functionality by reliably operating an electric fan while sustaining consistent voltage levels (Fig. 6(h) and Fig. S26 in the ESM). This performance highlights the device's viability for practical energy storage solutions.

4 Conclusion

In summary, this study demonstrates a percent-level NHS additive as a core strategy to enhance the stability and reversibility of zinc metal anodes in AZIBs. The carbonyl groups of the NHS effectively displace H_2O from the Zn^{2+} solvation sheath and participate in the coordination structure, thereby facilitating Zn^{2+} desolvation. Simultaneously, NHS modulates water activity and adsorbs onto the zinc surface, promoting uniform electric field distribution, suppressing side reactions, and guiding preferential Zn deposition along the (002) plane. These synergistic mechanisms collectively contribute to enhanced electrochemical performance. Symmetric Zn||Zn cells achieve over 7500 hours of stable cycling at 1 $mA{\cdot}cm^{-2}$ and 1 $mAh{\cdot}cm^{-2}$, while Zn||V_2O_5 full cells retain 82.5% capacity after 7000 cycles. Given its low concentration requirement and ease of integration, the NHS additive represents a practical and scalable approach for high-performance aqueous zinc-ion batteries.

Acknowledgements

This work was supported by the National Natural Science Foundation of China (22172103). The electrochemical data were tested by an electrochemical workstation from Corrtest, Wuhan, China.

Electronic Supplementary Material Supplementary material (further details of the material, characterizations, and electrochemical tests, battery performance, etc.) is available in the online version of this article at https://doi.org/10.26599/NRE.2025.9120213.

Declaration of conflicting interests

The authors declare no conflicting interests regarding the content of this article.

Author Contributions

W. X. S. proposed and designed the research. L. H. conducted the synthesis of the cathode and the complete cell assembly. L. H., X. X. C., D. M. M., H. Q. Z., and J. C. T. conducted the characterization and electrochemical measurements. L. H., W. X. S. conducted data analysis and contributed to manuscript writing. All authors reviewed findings and provided manuscript feedback.

Data availability

All data needed to support the conclusions in the paper are presented in the manuscript and/or the Supplementary Materials. Additional data related to this paper may be requested from the corresponding author upon request.

References

[1] Chen, S. M.; Peng, C.; Xue, D. F.; Ma, L. T.; Zhi, C. Y. Alkaline tolerant antifreezing additive enabling aqueous Zn||Ni battery operating at –60 °C. *Angew. Chem., Int. Ed.* **2022**, *61*, e202212767.

[2] Cui, Y. H.; Zhao, Q. H.; Wu, X. J.; Chen, X.; Yang, J. L.; Wang, Y. T.; Qin, R. Z.; Ding, S. X.; Song, Y. L.; Wu, J. W. et al. An interface-bridged organic-inorganic layer that suppresses dendrite formation and side reactions for ultra-long-life aqueous zinc metal anodes. *Angew. Chem., Int. Ed.* **2020**, *59*, 16594–16601.

[3] Ding, X. D.; Liu, F. Z.; Xu, Y. T.; Pei, Y.; Chen, L. J.; Wu, X. W.; Long, B. Low volume fraction co-solvent electrolyte regulates the solvation structure for highly stable zinc-ion batteries. *Mater. Today Energy* **2024**, *45*, 101697.

[4] Chen, H. G.; Guo, Z. C.; Wang, H. S.; Huang, W. Y.; Pan, F.; Wang, Z. Q. A liquid metal interlayer for boosted charge transfer and dendrite-free deposition toward high-performance Zn anodes. *Energy Storage Mater.* **2023**, *54*, 563–569.

[5] Chen, J. Y.; Zhao, Y. H.; Yang, X.; Tan, L. C.; Wu, X. L.; Chen, C. X. Recent advances in MXene materials for zinc-ion hybrid capacitors. *Nano Res. Energy* **2025**, *4*, e9120154.

[6] Dou, Q. Y.; Yao, N.; Pang, W. K.; Park, Y.; Xiong, P. X.; Han, X. T.; Rana, H. H.; Chen, X.; Fu, Z. H.; Thomsen, L. et al. Unveiling solvation structure and desolvation dynamics of hybrid electrolytes for ultralong cyclability and facile kinetics of Zn–Al alloy anodes. *Energy Environ. Sci.* **2022**, *15*, 4572–4583.

[7] Feng, D. D.; Jiao, Y. C.; Wu, P. Y. Guiding Zn uniform deposition with polymer additives for long-lasting and highly utilized Zn metal anodes. *Angew. Chem., Int. Ed.* **2023**, *62*, e202314456.

[8] Bai, S.; Wu, Z. H.; Zhang, X. X.; Qiu, J. K.; Chen, J. T.; Liu, Z. P.; Zhang, Y. N. Bifunctional electrolyte additive enabling long cycle life of vanadium-based cathode aqueous zinc ion batteries. *Chem. Eng. J.* **2024**, *500*, 157281.

[9] Cai, Z. W.; Wang, H.; Wu, T. Q.; Ji, H. M.; Tang, Y. G.; Zhang, Q.; Peng, Z. G.; Wang, H. Y. Accelerating Zn^{2+} kinetics and regulating zinc anode interface for high stable aqueous zinc-ion batteries. *Mater. Today Energy* **2024**, *43*, 101592.

[10] Feng, D. D.; Jiao, Y. C.; Wu, P. Y. Proton-reservoir hydrogel electrolyte for long-term cycling Zn/PANI batteries in wide temperature range. *Angew. Chem., Int. Ed.* **2023**, *62*, e202215060.

[11] Huang, C.; Zhao, X.; Liu, S.; Hao, Y. S.; Tang, Q. L.; Hu, A. P.; Liu, Z. X.; Chen, X. H. Stabilizing zinc anodes by regulating the electrical double layer with saccharin anions. *Adv. Mater.* **2021**, *33*, 2100445.

[12] Huang, T. Q.; Xu, K.; Jia, N.; Yang, L.; Liu, H. T.; Zhu, J. X.; Yan, Q. Y. Intrinsic interfacial dynamic engineering of zincophilic microbrushes via regulating Zn deposition for highly reversible aqueous zinc ion battery. *Adv. Mater.* **2023**, *35*, 2205206.

[13] Li, H. Y.; Ren, Y.; Zhu, Y.; Tian, J. M.; Sun, X. Y.; Sheng, C. C.; He, P.; Guo, S. H.; Zhou, H. S. A bio-inspired trehalose additive for reversible zinc anodes with improved stability and kinetics. *Angew. Chem., Int. Ed.* **2023**, *62*, e202310143.

[14] Xiao, T.; Yang, J. L.; Chao, D. L.; Fan, H. J. Multimodal electrolyte

architecting for static aqueous zinc-halogen batteries. *Natl. Sci. Rev.* **2025**, *12*, nwaf029.
[15] Lv, Z. H.; Kang, Y. H.; Chen, G. H.; Yang, J.; Chen, M. H.; Lin, P. X.; Wu, Q. L.; Zhang, M. H.; Zhao, J. B.; Yang, Y. Stable solid-state zinc-iodine batteries enabled by an inorganic $ZnPS_3$ solid electrolyte with interconnected Zn^{2+} migration channels. *Adv. Funct. Mater.* **2024**, *34*, 2310476.
[16] Qiu, M. J.; Sun, P.; Cui, G. F.; Mai, W. J. Chaotropic polymer additive with ion transport tunnel enable dendrite-free zinc battery. *ACS Appl. Mater. Interfaces* **2022**, *14*, 40951–40958.
[17] Qiu, M. J.; Sun, P.; Wang, Y.; Ma, L.; Zhi, C. Y.; Mai, W. J. Anion-trap engineering toward remarkable crystallographic reorientation and efficient cation migration of Zn ion batteries. *Angew. Chem., Int. Ed.* **2022**, *61*, e202210979.
[18] Liu, D. H.; Wang, A.; Liu, Y. Z.; Xu, F.; Luo, D.; Zheng, J. L.; Song, M. Q.; Xu, C. Y.; Chen, Z. W. V-O-Ru heterogeneous interphase reversible reconstruction endowing $Zn_{0.85}V_{10}O_{24}{\cdot}7.4H_2O/0.65RuO_2$ cathode robust H^+/Zn^{2+} storage. *Adv. Mater.* **2025**, *37*, 2501624.
[19] Liu, D. H.; Xu, C. Y.; Xu, F.; Liu, Y. Z.; Wang, A.; Yun, C.; Song, M. Q.; Zheng, J. L.; Wang, L. Interphase synergy achieving stable cycling performance for aqueous Zn-MnO_2 battery. *Carbon Neutral.* **2025**, *4*, e70014.
[20] Zhou, T.; Han, X.; Shen, W. W.; Ji, F.; Liu, M. L.; Song, Y. Y.; He, W. W. Construction of NiS/CTF heterojunction photocatalyst with an outstanding photocatalytic hydrogen evolution performance. *Chin. Chem. Lett.* **2025**, *36*, 110415.
[21] Sun, P.; Ma, L.; Zhou, W. H.; Qiu, M. J.; Wang, Z. L.; Chao, D. L.; Mai, W. J. Simultaneous regulation on solvation shell and electrode interface for dendrite-free Zn ion batteries achieved by a low-cost glucose additive. *Angew. Chem., Int. Ed.* **2021**, *60*, 18247–18255.
[22] Tian, H. J.; Feng, G. X.; Wang, Q.; Li, Z.; Zhang, W.; Lucero, M.; Feng, Z. X.; Wang, Z. L.; Zhang, Y. N.; Zhen, C. et al. Three-dimensional Zn-based alloys for dendrite-free aqueous Zn battery in dual-cation electrolytes. *Nat. Commun.* **2022**, *13*, 7922.
[23] Wan, F.; Zhang, L. L.; Dai, X.; Wang, X. Y.; Niu, Z. Q.; Chen, J. Aqueous rechargeable zinc/sodium vanadate batteries with enhanced performance from simultaneous insertion of dual carriers. *Nat. Commun.* **2018**, *9*, 1656.
[24] Wang, Y. Y.; Ren, T. T.; Wang, Z. P.; Liu, C. X.; Zhang, Y. H.; Xu, A.; Chen, C. X.; Bai, J. B.; Wang, H.; Liu, X. J. Enabling and boosting preferential epitaxial zinc growth via multi-interface regulation for stable and dendrite-free zinc metal batteries. *Adv. Energy Mater.* **2024**, *14*, 2400613.
[25] Yan, C.; He, F. Z.; Feng, L. K.; Zhu, L.; Li, P.; Tang, J.; He, H. B.; Liu, Y.; Zhu, Y. Q.; Li, G. H. et al. Interfacial molecule engineering builds tri-functional bilayer silane films with hydrophobic ion channels for highly stable Zn metal anode. *Adv. Funct. Mater.* **2025**, *35*, 2503493.
[26] Xie, X. F.; Deng, L. F.; Li, L. Y.; Pan, A. Q.; Liang, S. Q.; Fang, G. Z. Modulating interfacial Zn^{2+} deposition mode towards stable Zn anode via bimetallic co-doped coating. *Energy Storage Mater.* **2024**, *73*, 103834.
[27] Ren, Q. Q.; Tang, X. Y.; Guo, Y. Q.; Liao, X. B.; Zhang, C. M.; Zhu, Z. X.; Wang, P. P.; Wang, W.; Li, Y.; Song, W. J. et al. Achieving the dendrite-free Zn anode by inducing the (101)-preferred electrodeposition of Zn crystals. *Adv. Energy Mater.* **2025**, *15*, 2403961.
[28] Bie, Z.; Yang, Q.; Cai, X. X.; Chen, Z.; Jiao, Z. Y.; Zhu, J. B.; Li, Z. F.; Liu, J. Z.; Song, W. X.; Zhi, C. Y. One-step construction of a polyporous and zincophilic interface for stable zinc metal anodes. *Adv. Energy Mater.* **2022**, *12*, 2202683.
[29] Cai, X. X.; Wang, X. X.; Bie, Z.; Jiao, Z. Y.; Li, Y. R.; Yan, W.; Fan, H. J.; Song, W. X. A layer-by-layer self-assembled bio-macromolecule film for stable zinc anode. *Adv. Mater.* **2024**, *36*, 2306734.
[30] Li, Y. R.; Zhang, M. Q.; Lu, H. B.; Cai, X. X.; Jiao, Z. Y.; Li, S. J.; Song, W. X. Boosting high-performance aqueous zinc-ion hybrid capacitors via organic redox species on laser-induced graphene network. *Adv. Funct. Mater.* **2024**, *34*, 2400663.
[31] Wang, D. D.; Lv, D.; Liu, H. X.; Zhang, S. J.; Wang, C.; Wang, C. T.; Yang, J.; Qian, Y. T. *In situ* formation of nitrogen-rich solid electrolyte interphase and simultaneous regulating solvation structures for advanced Zn metal batteries. *Angew. Chem., Int. Ed.* **2022**, *61*, e202212839.
[32] Wang, J. L.; Gao, X. Y.; Wang, Y. W.; Pan, R. N.; Liu, Z.; Liu, X.; Xie, H. J.; Yu, F.; Wang, G.; Gu, T. T. Robust ring insoluble naphthoquinone derivative cathode with high loading and long cycle life for aqueous zinc organic batteries. *Nano Res. Energy* **2024**, *3*, e9120124.
[33] Yang, J. L.; Li, J.; Zhao, J. W.; Liu, K.; Yang, P. H.; Fan, H. J. Stable zinc anodes enabled by a zincophilic polyanionic hydrogel layer. *Adv. Mater.* **2022**, *34*, 2202382.
[34] Zeng, X. H.; Mao, J. F.; Hao, J. N.; Liu, J. T.; Liu, S. L.; Wang, Z. J.; Wang, Y. Y.; Zhang, S. L.; Zheng, T.; Liu, J. W. et al. Electrolyte design for *in situ* construction of highly Zn^{2+}-conductive solid electrolyte interphase to enable high-performance aqueous Zn-ion batteries under practical conditions. *Adv. Mater.* **2021**, *33*, 2007416.
[35] Wu, J. W.; Yang, J. L.; Zhang, B.; Fan, H. J. Immobilizing polyiodides with expanded Zn^{2+} channels for high-rate practical zinc-iodine battery. *Adv. Energy Mater.* **2024**, *14*, 2302738.
[36] Zhang, L.; Wu, J. W.; Lu, T. T.; Li, X. Y.; Wu, H.; Chen, T.; Zhang, Y. L.; Wei, J. T.; Hu, M. G.; Zheng, X. M. et al. Improving Zn^{2+} migration via designing multiple zincophilic polymer electrolyte for advanced aqueous zinc ion batteries. *Chem. Eng. J.* **2024**, *496*, 153815.
[37] Zhou, J.; Shan, L. T.; Wu, Z. X.; Guo, X.; Fang, G. Z.; Liang, S. Q. Investigation of V_2O_5 as a low-cost rechargeable aqueous zinc ion battery cathode. *Chem. Commun.* **2018**, *54*, 4457–4460.
[38] Frisch, M. J.; Trucks, G. W.; Schlegel, H. B.; Scuseria, G. E.; Robb, M. A.; Cheeseman, J. R.; Scalmani, G.; Barone, V.; Petersson, G. A.; Nakatsuji, H. et al. GaussView 5.0. Wallingford: E.U.A., 2016.
[39] Wang, Y. L.; Shah, F. U.; Glavatskih, S.; Antzutkin, O. N.; Laaksonen, A. Atomistic insight into orthoborate-based ionic liquids: Force field development and evaluation. *J. Phys. Chem. B* **2014**, *118*, 8711–8723.
[40] Abraham, M. J.; Murtola, T.; Schulz, R.; Páll, S.; Smith, J. C.; Hess, B.; Lindahl, E. GROMACS: High performance molecular simulations through multi-level parallelism from laptops to supercomputers. *SoftwareX* **2015**, *1–2*, 19–25.
[41] Kresse, G.; Hafner, J. *Ab initio* molecular dynamics for liquid metals. *Phys. Rev. B* **1993**, *47*, 558–561.
[42] Kresse, G.; Joubert, D. From ultrasoft pseudopotentials to the projector augmented-wave method. *Phys. Rev. B* **1999**, *59*, 1758–1775.
[43] Zhang, Q.; Luan, J. Y.; Fu, L.; Wu, S. G.; Tang, Y. G.; Ji, X. B.; Wang, H. Y. The three-dimensional dendrite-free zinc anode on a copper mesh with a zinc-oriented polyacrylamide electrolyte additive. *Angew. Chem., Int. Ed.* **2019**, *58*, 15841–15847.
[44] Zheng, X. H.; Xu, K.; Ma, Y. R.; Sun, J. F.; Han, B. B.; Luo, R. H.; Wang, M. M.; Chen, N.; Song, L.; Zhao, Q. B. et al. Development of durable Zn-MnO_2 battery via a functionalized hydrogel film. *Adv. Energy Mater.* **2024**, *14*, 2400038.
[45] Zhong, Y.; Cheng, Z. X.; Zhang, H. W.; Li, J. B.; Liu, D. D.; Liao, Y. Q.; Meng, J. T.; Shen, Y.; Huang, Y. H. Monosodium glutamate, an effective electrolyte additive to enhance cycling performance of Zn anode in aqueous battery. *Nano Energy* **2022**, *98*, 107220.
[46] Zhou, L. J.; Wang, F. X.; Yang, F.; Liu, X. Q.; Yu, Y. X.; Zheng, D. Z.; Lu, X. H. Unshared pair electrons of zincophilic Lewis base enable long-life Zn anodes under "three high" conditions. *Angew. Chem., Int. Ed.* **2022**, *61*, e202208051.
[47] Zhu, J. B.; Bie, Z.; Cai, X. X.; Jiao, Z. Y.; Wang, Z. T.; Tao, J. C.; Song, W. X.; Fan, H. J. A molecular-sieve electrolyte membrane enables separator-free zinc batteries with ultralong cycle life. *Adv. Mater.* **2022**, *34*, 2207209.
[48] Zong, Q.; Lv, B.; Liu, C. F.; Yu, Y. F.; Kang, Q. L.; Li, D. Y.; Zhu, Z. J.; Tao, D. W.; Zhang, J. J.; Wang, J. Y. et al. Dendrite-free and highly stable Zn metal anode with $BaTiO_3$/P(VDF-TrFE) coating. *ACS Energy Lett.* **2023**, *8*, 2886–2896.

Liang Huang is currently a graduate student at Capital Normal University. His research interests focus on aqueous zinc ion batteries.

Weixing Song received her PhD from the Institute of Chemistry at the Chinese Academy of Sciences. During her doctoral studies, she was also a joint-training graduate student at the Max Planck Institute of Colloids and Interfaces in Germany. She is currently a full professor and doctoral supervisor in the Department of Chemistry at Capital Normal University. Her major research focuses on environmental energy conversion and storage.